Cite as: J. Mao *et al.*, *Science* 10.1126/science.aax7792 (2019).

# High thermoelectric cooling performance of n-type $Mg_3Bi_2$-based materials

**Jun Mao[1], Hangtian Zhu[1], Zhiwei Ding[2], Zihang Liu[1], Geethal Amila Gamage[1], Gang Chen[2]*, Zhifeng Ren[1]***

[1]Department of Physics and Texas Center for Superconductivity (TcSUH), University of Houston, Houston, TX 77204, USA. [2]Department of Mechanical Engineering, Massachusetts Institute of Technology, Cambridge, MA 02139, USA.

***Corresponding author. Email: gchen2@mit.edu (G.C.); zren@uh.edu (Z.R.)**

**Thermoelectric materials have a large Peltier effect, making them attractive materials for solid-state cooling applications. $Bi_2Te_3$-based alloys have remained as the state-of-the-art room temperature materials for many decades. However, cost partially limited wider use of thermoelectric cooling devices because of the large amounts of expensive tellurium. We report n-type $Mg_3Bi_2$-based materials with a peak *ZT* of ~0.9 at 350 K, which is comparable to the commercial $Bi_2Te_{3-x}Se_x$, but much cheaper. A cooling device made of our material and p-type $Bi_{0.5}Sb_{1.5}Te_3$ has produced a large temperature difference of ~91 K at the hot-side temperature of 350 K. The n-type $Mg_3Bi_2$-based materials are promising for thermoelectric cooling applications.**

Thermoelectric modules can directly convert electricity into thermal energy for cooling and heating and harvest waste heat for electrical power (*1*, *2*). The global thermoelectric module market was worth ~0.6 billion US dollars in 2018 and it is anticipated to reach ~1.7 billion US dollars by 2027 (*3*). Most thermoelectric modules have been used for thermal management since the market for power generation is still in its infancy. The cooling capability of a thermoelectric module largely relies on the performance of the materials used. The performance is governed by the dimensionless figure of merit $ZT = S^2\rho^{-1}\kappa^{-1}T$, where $S$ is the Seebeck coefficient, $\rho$ the electrical resistivity, $\kappa$ the thermal conductivity, and $T$ the absolute temperature (*4*–*6*). Although advancements have been made on mid- and high-$T$ materials, e.g., lead chalcogenides (*7*, *8*), Skutterudites (*9*, *10*), $Mg_2Sn$-based materials (*11*, *12*), SnSe (*13*, *14*), and half-Heuslers (*15*–*17*), the progress on room-temperature (*RT*) materials is sluggish. N-type $Bi_2Te_{3-x}Se_x$ and p-type $Bi_{2-x}Sb_xTe_3$ remained as the state-of-the-art *RT* thermoelectric materials for the past several decades. Even though enhancements in the thermoelectric performance of nanostructured n-type $Bi_2Te_{3-x}Se_x$ were reported (*18*, *19*), it is challenging to minimize the electrical contact resistance between the contact material and $Bi_2Te_{3-x}Se_x$ (*20*) on top of the anisotropy issue of $Bi_2Te_{3-x}Se_x$ (*18*). Despite the progress made on materials, they have not been engineered into viable thermoelectric cooling applications yet. Additionally, the high cost of tellurium (Te) partially limits the wider applications of thermoelectric modules. Identifying new materials with high *ZT*, low cost, and easy to minimize the contact resistance is essential for the widespread use of thermoelectric cooling modules.

We report the n-type $Mg_3Bi_2$-based materials with high *ZT* around 300 K. We constructed a unicouple consisting of n-type $Mg_{3.2}Bi_{1.498}Sb_{0.5}Te_{0.002}$ and p-type $Bi_{0.5}Sb_{1.5}Te_3$ (Fig. 1A) and measured the cooling performance (Fig. 1B) (*21*). The Peltier effect (*2*) allows us to remove heat from the top, cold-side, copper plate and dissipates it into the bottom, hot-side, copper blocks by applying an electrical current. This results in a $T$ difference between the hot and cold sides (Fig. 1B). This effect increased with increasing current until it eventually saturated at 91 K with the hot-side $T$ maintained at 350 K. We found the hot-side $T$ dependent maximum $T$ difference ($\Delta T$) was higher for our unicouple when compared to the commercial data (Fig. 1B, inset). Different from the nanostructured $Bi_2Te_{3-x}Se_x$ that has contact issue, we found Fe and Ni were both good contact materials for $Mg_{3.2}Bi_2$-based materials (fig. S2) and fabrication of $Mg_{3.2}Bi_{1.498}Sb_{0.5}Te_{0.002}$ leg with contact materials was easy (*21*). Our $Mg_{3.2}Bi_2$-based materials should be much cheaper than $Bi_2Te_{3-x}Se_x$ as they minimize the need for expensive Te. The cost of thermoelectric materials makes up nearly one third of the total cost for thermoelectric modules (*22*). Replacing $Bi_2Te_{3-x}Se_x$ with the $Mg_3Bi_2$-based materials should effectively reduce the cost of thermoelectric modules and potentially expand their usefulness for various cooling applications.

N-type $Mg_3Sb_2$-based materials with promising thermoelectric performance were reported recently (*23*–*33*), mainly targeted for power generation from waste heat. Unlike the semiconducting $Mg_3Sb_2$, the isostructural $Mg_3Bi_2$ is a semimetal (*34*–*36*). We found stoichiometry $Mg_3Bi_2$ showed p-type conduction (fig. S3B), in agreement with other measurements (*34*, *35*). We attributed the p-type conduction to the presence of a high concentration of Mg vacancies, similar to $Mg_3Sb_2$ (*23*, *29*). We successfully synthesized n-type $Mg_3Bi_2$ samples

with excess Mg, *i.e.*, $Mg_{3+\delta}Bi_2$ ($\delta$ = 0.05, 0.1, and 0.2). The thermoelectric properties of these samples were very similar to one another (fig. S3). We focused on $Mg_{3.2}Bi_2$ and its carrier concentration ($n$) was ~$2.1\times10^{19}$ $cm^{-3}$ at 10 K (Fig. 2A, upper panel). Carrier concentration noticeably increased once $T$ was above 150 K. Below 300 K the carrier mobility ($\mu$) was more than 200 $cm^2\ V^{-1}\ s^{-1}$ and reached a high value of ~4198 $cm^2\ V^{-1}\ s^{-1}$ at 10 K (Fig. 2A, lower panel). The high $n$ and $\mu$ in conjunction with the low bipolar conduction $T$ clearly indicated the semi-metallic characteristic of $Mg_{3.2}Bi_2$. Electrical resistivity of $Mg_{3.2}Bi_2$ was only ~9 $\mu\Omega$ m at 300 K and ~0.58 $\mu\Omega$ m at 2 K (Fig. 2B). Seebeck coefficient of $Mg_{3.2}Bi_2$ was ~-105 $\mu V\ K^{-1}$ at 300 K and more than -80 $\mu V\ K^{-1}$ over a broad $T$ range between 130 K and 350 K. The power factor ($S^2\rho^{-1}$) of $Mg_{3.2}Bi_2$ was ~10 $\mu W\ cm^{-1}\ K^{-2}$ across a broad $T$ range (Fig. 2D). Doping the samples with a small amount of Te effectively modulated $n$ of $Mg_{3.2}Bi_2$ (fig. S4A), reducing $\rho$ and slightly enhancing $S$ (Fig. 2, B and C, respectively). This resulted in substantially higher $S^2\rho^{-1}$ on the order of ~20 $\mu W\ cm^{-1}\ K^{-2}$ over a broad $T$ range (Fig. 2D). We obtained a peak $ZT$ ~0.3 at 350 K with $Mg_{3.2}Bi_{1.998}Te_{0.002}$ and above 0.1 down to 150 K (fig. S5B).

Semimetals usually have a low Seebeck coefficient due to cancellation between electrons and holes, but the n-type $Mg_{3.2}Bi_2$ studied here has a large $S$, which is essential for its high thermoelectric performance. To understand the origin of the large $S$, we calculated the band structure of $Mg_3Bi_2$ (fig. S6A). The band overlap energy we calculated between the conduction band minimum and valence band maximum was ~-0.4 eV. However, the two-band modelling estimated this at ~-0.1 eV (fig. S7). We rigidly shifted band structure with the band overlap energy shifted to -0.1 eV (Fig. 3A). The conduction band minimum located along the L-M line with the valley degeneracy of 6 (fig. S8A) and the valence band maximum located around $\Gamma$ point with the valley degeneracy of 1 (fig. S8B). Different band structures were previously reported for $Mg_3Bi_2$ (*24*, *36*, *37*) due to the choice of pseudo-potential and whether the spin-orbital coupling was considered (*36*, *37*). Due to the presence of electrons and holes in a semi-metal, we expressed $S$ as $S = \left(\rho_h S_e + \rho_e S_h\right)/\left(\rho_e + \rho_h\right)$, where $S_e$ and $S_h$ were partial $S$ for electrons and holes, respectively, and $\rho_e$ and $\rho_h$ were partial $\rho$ for electrons and holes, respectively. We applied a two-band model to calculate the partial $S$ and $\mu$ for $Mg_{3.2}Bi_2$. We found the partial $S$ for electrons was noticeably larger than that of the holes (Fig. 3B). We attributed the difference in the partial $S$ to the disparity in density-of-states effective mass $m_d^*$, ~$0.530m_0$ ($m_0$ is the free electron mass) for the conduction band and ~$0.276m_0$ for the valence band (table S1). Density-of-states effective mass depends on the band effective mass ($m^*$) and the valley degeneracy ($N$) according to $m_d^* = N^{2/3}m^*$ (*38*). The different $N$ in the conduction and valence bands (fig. S8) accounts for the disparity in $m_d^*$. We also modeled the partial $\mu$ of $Mg_{3.2}Bi_2$ between 100 K and 350 K (Fig. 3C). We omitted the values under 100 K because they have relatively large uncertainties. Our modeling showed that the electrons have higher $\mu$ than that of the holes. Carrier mobility is proportional to $\left(m^*\right)^{-3/2}\left(m_I^*\right)^{-1}$ when acoustic phonon scattering is the predominant scattering process and $m_I^*$ is the inertial effective mass (*38*). Based on the density functional theory results, we extracted from the model $m^*$ ~$0.161m_0$ for electrons and ~$0.276m_0$ for holes and the $m_I^*$ was ~$0.133m_0$ for electrons, and ~$0.259m_0$ for holes (table S1). The differences in the effective masses between conduction and valence bands explained the disparity in $\mu$ between electrons and holes. We can quantify the asymmetrical transport properties between the conduction and valence bands by the electron-to-hole weighted mobility ratio $A = \left(N_e m_e^{*3/2}\mu_e\right)/\left(N_h m_h^{*3/2}\mu_h\right)$ (*5*, *39*–*41*). When the transport properties were highly asymmetrical, *i.e.*, $A >> 1$ or $A << 1$, a large $S$ at 300 K can be achieved for semi-metals and semiconductors with small $E_g$ (figs. S10 and S11). The calculated electron-to-hole mobility ratio was around 3 and $A$ was above 8 for $Mg_{3.2}Bi_2$ (Fig. 3D). The large $A$ contributed to the high $S$ of n-type $Mg_{3.2}Bi_2$. Meanwhile, it partially explained why p-type $Mg_3Bi_2$ has a much lower $S$ and inferior thermoelectric performance (fig. S3). The large $S$ in n-type $Mg_{3.2}Bi_2$ is similar to that in single-crystal bismuth, which has an electron-to-hole mobility ratio of ~9.19 along the trigonal axis (*42*–*44*), $m_d^*$ ~$0.113m_0$ for electrons, and $m_d^*$ ~$0.093m_0$ for holes (*44*). As a result, $A$ was as large as ~11 along the trigonal axis for bismuth, and thus a high $S$ of ~-100 $\mu V\ K^{-1}$ at 300 K along this direction.

The relatively high $\kappa$ of $Mg_{3.2}Bi_2$ limited the thermoelectric performance (fig. S5A). Partial substitution of Bi with Sb in $Mg_{3.2}Bi_2$ should substantially reduce the lattice thermal conductivity ($\kappa_{lat}$). We prepared a range of sample with Sb, $Mg_{3.2}Bi_{1.998-x}Sb_xTe_{0.002}$ ($x$ = 0, 0.1, 0.3, 0.5, and 0.7). Increased Sb concentration increased $\rho$ of $Mg_{3.2}Bi_{1.998-x}Sb_xTe_{0.002}$ (Fig. 4A). We measured $\rho$ ~8.1 $\mu\Omega$ m at 300 K and ~2.2 $\mu\Omega$ m at 2 K for $Mg_{3.2}Bi_{1.998}Te_{0.002}$. In comparison, we measured $\rho$ ~24.4 $\mu\Omega$ m at 300 K and ~9.9 $\mu\Omega$ m at 2 K for $Mg_{3.2}Bi_{1.298}Sb_{0.7}Te_{0.002}$. We attributed the increased $\rho$ to the reduced $n$ (fig. S13A) and $\mu$ (fig. S13B) after Sb alloying. Similarly, Sb alloying greatly enhanced $S$ (Fig. 4B). Room-temperature $S$ was ~-129 $\mu V\ K^{-1}$ for $Mg_{3.2}Bi_{1.998}Te_{0.002}$ and ~-229 $\mu V\ K^{-1}$ for $Mg_{3.2}Bi_{1.298}Sb_{0.7}Te_{0.002}$. We ascribed the enhancement of $S$ mainly to the reduced $n$ (fig. S13A). In addition, the modified band structure after Sb alloying partially influenced the $T$-dependence of $S$. Because $Mg_3Bi_2$ is a semi-metal while $Mg_3Sb_2$ is a semiconductor, we expected a band structure

transition from semi-metallic to semiconducting in $Mg_{3.2}Bi_{1.998-x}Sb_xTe_{0.002}$ solid solutions. To probe the variation in band structure after Sb alloying, we measured the *T*-dependent ρ of undoped $Mg_{3.2}Bi_{2-x}Sb_x$ ($x$ = 0, 0.1, 0.2, 0.3, 0.4, 0.5, 0.6, and 0.7). We described this with $\rho = \rho_{300K} \exp\left(E_g / 2k_BT\right)$ (*45*) (Fig. 4D and fig. S15). We found a clear semi-metallic to semiconducting transition with increasing Sb concentration. We determined an $E_g$ ~-0.013 eV for $Mg_{3.2}Bi_2$ and $Mg_{3.2}Bi_{1.9}Sb_{0.1}$ showed a nearly zero $E_g$ (~0.005 eV). All of the samples with Sb concentration of more than 5% ($x$ > 0.1) were semiconducting and $E_g$ increased with greater Sb concentration. The reported $E_g$ of $Mg_{3+\delta}Bi_{0.89}Sb_{1.1}Te_{0.01}$ was ~0.240 eV (*32*) and that of $Mg_{3.2}Bi_{1.3}Sb_{0.7}$ was ~0.147 eV. The lower $E_g$ is reasonable because we have a lower Sb concentration. An $E_g$ value of -0.013 eV estimated from the temperature dependence of ρ for $Mg_{3.2}Bi_2$ is slightly smaller than the value we estimated from the two-band modelling of ~-0.10 eV (Fig. 3A and fig. S7). This suggests the band overlap energy of $Mg_3Bi_2$ should be small, but require high quality single crystal measurements to completely resolve.

We can also understand the transition after Sb alloying from the variation in *T*-dependent *n* (fig. S13A). Carrier concentration of $Mg_{3.2}Bi_{1.998}Te_{0.002}$ and $Mg_{3.2}Bi_{1.898}Sb_{0.1}Te_{0.002}$ increased noticeably with *T* above 125 K due to the activation of electron-hole pairs from bipolar conduction. This phenomenon was greatly suppressed in $Mg_{3.2}Bi_{1.698}Sb_{0.3}Te_{0.002}$ and finally minimized in $Mg_{3.2}Bi_{1.498}Sb_{0.5}Te_{0.002}$ and $Mg_{3.2}Bi_{1.298}Sb_{0.7}Te_{0.002}$. In addition, the reduced *n* in $Mg_{3.2}Bi_{1.998-x}Sb_xTe_{0.002}$ with increasing Sb concentration also indicated the downward shift of the Fermi energies due to upward movement of conduction band edges that opened $E_g$. Despite the semi-metal to semiconductor transition after Sb alloying, the $S^2\rho^{-1}$ among $Mg_{3.2}Bi_{1.998-x}Sb_xTe_{0.002}$ samples were comparable (Fig. 4C). We observed a slight enhancement in $S^2\rho^{-1}$ in $Mg_{3.2}Bi_{1.898}Sb_{0.1}Te_{0.002}$ ($E_g$ ~0.005 eV) and $Mg_{3.2}Bi_{1.698}Sb_{0.3}Te_{0.002}$ ($E_g$ ~0.063 eV) compared to $Mg_{3.2}Bi_{1.998}Te_{0.002}$. Power factors at lower *T* were reduced due to the substantially reduced μ when the Sb concentration was above 25% ($x$ > 0.5) (fig. S13B). We observed a substantial reduction in κ of $Mg_{3.2}Bi_{1.998-x}Sb_xTe_{0.002}$ with increasing Sb concentration (fig. S15). We attributed this reduction to the substantially reduced $\kappa_{lat}$ due to alloying scattering (Fig. 4E). The peak $\kappa_{lat}$ around 20 K was as high as ~9.6 W m$^{-1}$ K$^{-1}$ for $Mg_{3.2}Bi_{1.998}Te_{0.002}$ and only ~3.2 W m$^{-1}$ K$^{-1}$ for $Mg_{3.2}Bi_{1.298}Sb_{0.7}Te_{0.002}$. The reduced $\kappa_{lat}$ translated into an enhanced *ZT* (Fig. 4F). The *ZT* at 350 K was ~0.3 for $Mg_{3.2}Bi_{1.998}Te_{0.002}$ and ~0.9 for $Mg_{3.2}Bi_{1.498}Sb_{0.5}Te_{0.002}$. Although the thermoelectric performance of $Mg_{3.2}Bi_{1.998-x}Sb_xTe_{0.002}$ decreased with reduced *T*, both $Mg_{3.2}Bi_{1.498}Sb_{0.5}Te_{0.002}$ and $Mg_{3.2}Bi_{1.298}Sb_{0.7}Te_{0.002}$ maintained a *ZT* above 0.3 down to 200 K. The average *ZT* between 200 K and 350 K was ~0.6 for $Mg_{3.2}Bi_{1.298}Sb_{0.7}Te_{0.002}$, ~0.6 for $Mg_{3.2}Bi_{1.498}Sb_{0.5}Te_{0.002}$, and ~0.2 for $Mg_{3.2}Bi_{1.998}Te_{0.002}$. We measured the commercial n-type $Bi_2Te_{3-x}Se_x$ ingot and it showed a *ZT* of ~0.85 at 350 K, comparable to our $Mg_{3.2}Bi_{1.998-x}Sb_xTe_{0.002}$ (fig. S17). However, the commercial $Bi_2Te_{3-x}Se_x$ ingot showed a strong anisotropy in the thermoelectric properties due its highly preferred orientation. This requires the thermoelectric legs to be cut along the direction with better performance. In contrast, our $Mg_{3.2}Bi_2$-based materials have nearly isotropic thermoelectric properties and the leg fabrication will be easier. In addition, our $Mg_{3.2}Bi_2$-based materials are mechanically robust while the commercial $Bi_2Te_{3-x}Se_x$ ingot can easily delaminate from the cleavage plane. Further enhancements in the thermoelectric properties of $Mg_3Bi_2$-based are very likely, e.g., improving μ and reducing $\kappa_{lat}$. Therefore, our n-type $Mg_3Bi_2$-based materials are highly attractive for thermoelectric cooling applications.

## REFERENCES AND NOTES


1. A. F. Ioffe, *Semiconductor Thermoelements and Thermoelectric Cooling* (Infosearch, 1957).
2. H. Goldsmid, *Thermoelectric Refrigeration* (Springer, 1964).
3. Transparency Market Research (2019); www.transparencymarketresearch.com/.
4. J. He, T. M. Tritt, Advances in thermoelectric materials research: Looking back and moving forward. *Science* **357**, eaak9997 (2017). doi:10.1126/science.aak9997 Medline
5. J. Mao, Z. Liu, J. Zhou, H. Zhu, Q. Zhang, G. Chen, Z. Ren, Advances in thermoelectrics. *Adv. Phys.* **67**, 69–147 (2018). doi:10.1080/00018732.2018.1551715
6. I. Petsagkourakis, K. Tybrandt, X. Crispin, I. Ohkubo, N. Satoh, T. Mori, Thermoelectric materials and applications for energy harvesting power generation. *Sci. Technol. Adv. Mater.* **19**, 836–862 (2018). doi:10.1080/14686996.2018.1530938 Medline
7. J. P. Heremans, V. Jovovic, E. S. Toberer, A. Saramat, K. Kurosaki, A. Charoenphakdee, S. Yamanaka, G. J. Snyder, Enhancement of thermoelectric efficiency in PbTe by distortion of the electronic density of states. *Science* **321**, 554–557 (2008). doi:10.1126/science.1159725 Medline
8. Y. Pei, X. Shi, A. LaLonde, H. Wang, L. Chen, G. J. Snyder, Convergence of electronic bands for high performance bulk thermoelectrics. *Nature* **473**, 66–69 (2011). doi:10.1038/nature09996 Medline
9. X. Shi, J. Yang, J. R. Salvador, M. Chi, J. Y. Cho, H. Wang, S. Bai, J. Yang, W. Zhang, L. Chen, Multiple-filled skutterudites: High thermoelectric figure of merit through separately optimizing electrical and thermal transports. *J. Am. Chem. Soc.* **133**, 7837–7846 (2011). doi:10.1021/ja111199y Medline
10. W. Zhao, Z. Liu, Z. Sun, Q. Zhang, P. Wei, X. Mu, H. Zhou, C. Li, S. Ma, D. He, P. Ji, W. Zhu, X. Nie, X. Su, X. Tang, B. Shen, X. Dong, J. Yang, Y. Liu, J. Shi, Superparamagnetic enhancement of thermoelectric performance. *Nature* **549**, 247–251 (2017). doi:10.1038/nature23667 Medline
11. W. Liu, X. Tan, K. Yin, H. Liu, X. Tang, J. Shi, Q. Zhang, C. Uher, Convergence of conduction bands as a means of enhancing thermoelectric performance of n-type Mg2Si(1-x)Sn(x) solid solutions. *Phys. Rev. Lett.* **108**, 166601 (2012). doi:10.1103/PhysRevLett.108.166601 Medline
12. W. Liu, H. S. Kim, S. Chen, Q. Jie, B. Lv, M. Yao, Z. Ren, C. P. Opeil, S. Wilson, C.-W. Chu, Z. Ren, n-type thermoelectric material $Mg_2Sn_{0.75}Ge_{0.25}$ for high power generation. *Proc. Natl. Acad. Sci. U.S.A.* **112**, 3269–3274 (2015). doi:10.1073/pnas.1424388112 Medline
13. L.-D. Zhao, G. Tan, S. Hao, J. He, Y. Pei, H. Chi, H. Wang, S. Gong, H. Xu, V. P. Dravid, C. Uher, G. J. Snyder, C. Wolverton, M. G. Kanatzidis, Ultrahigh power factor and thermoelectric performance in hole-doped single-crystal SnSe. *Science* **351**, 141–144 (2016).
14. C. Chang, M. Wu, D. He, Y. Pei, C.-F. Wu, X. Wu, H. Yu, F. Zhu, K. Wang, Y. Chen, L.

Huang, J.-F. Li, J. He, L.-D. Zhao, 3D charge and 2D phonon transports leading to high out-of-plane *ZT* in n-type SnSe crystals. *Science* **360**, 778–783 (2018). doi:10.1126/science.aaq1479 Medline
15. C. Fu, S. Bai, Y. Liu, Y. Tang, L. Chen, X. Zhao, T. Zhu, Realizing high figure of merit in heavy-band p-type half-Heusler thermoelectric materials. *Nat. Commun.* **6**, 8144 (2015). doi:10.1038/ncomms9144 Medline
16. H. Zhu, R. He, J. Mao, Q. Zhu, C. Li, J. Sun, W. Ren, Y. Wang, Z. Liu, Z. Tang, A. Sotnikov, Z. Wang, D. Broido, D. J. Singh, G. Chen, K. Nielsch, Z. Ren, Discovery of ZrCoBi based half Heuslers with high thermoelectric conversion efficiency. *Nat. Commun.* **9**, 2497 (2018). doi:10.1038/s41467-018-04958-3 Medline
17. H. Zhu, J. Mao, Y. Li, J. Sun, Y. Wang, Q. Zhu, G. Li, Q. Song, J. Zhou, Y. Fu, R. He, T. Tong, Z. Liu, W. Ren, L. You, Z. Wang, J. Luo, A. Sotnikov, J. Bao, K. Nielsch, G. Chen, D. J. Singh, Z. Ren, Discovery of TaFeSb-based half-Heuslers with high thermoelectric performance. *Nat. Commun.* **10**, 270 (2019). doi:10.1038/s41467-018-08223-5 Medline
18. X. Yan, B. Poudel, Y. Ma, W. S. Liu, G. Joshi, H. Wang, Y. Lan, D. Wang, G. Chen, Z. F. Ren, Experimental studies on anisotropic thermoelectric properties and structures of n-type $Bi_2Te_{2.7}Se_{0.3}$. *Nano Lett.* **10**, 3373–3378 (2010). doi:10.1021/nl101156v Medline
19. L. Hu, H. Wu, T. Zhu, C. Fu, J. He, P. Ying, X. Zhao, Tuning Multiscale Microstructures to Enhance Thermoelectric Performance of n-Type Bismuth-Telluride-Based Solid Solutions. *Adv. Energy Mater.* **5**, 1500411 (2015). doi:10.1002/aenm.201500411
20. W. Liu, H. Wang, L. Wang, X. Wang, G. Joshi, G. Chen, Z. Ren, Understanding of the contact of nanostructured thermoelectric n-type Bi2Te2.7Se0.3 legs for power generation applications. *J. Mater. Chem. A Mater. Energy Sustain.* **1**, 13093–13100 (2013). doi:10.1039/c3ta13456c
21. See the supplementary materials.
22. S. LeBlanc, S. K. Yee, M. L. Scullin, C. Dames, K. E. Goodson, Material and manufacturing cost considerations for thermoelectrics. *Renew. Sustain. Energy Rev.* **32**, 313–327 (2014). doi:10.1016/j.rser.2013.12.030
23. H. Tamaki, H. K. Sato, T. Kanno, Isotropic Conduction Network and Defect Chemistry in $Mg_{3+\delta}Sb_2$ -Based Layered Zintl Compounds with High Thermoelectric Performance. *Adv. Mater.* **28**, 10182–10187 (2016). doi:10.1002/adma.201603955 Medline
24. J. Zhang, L. Song, S. H. Pedersen, H. Yin, L. T. Hung, B. B. Iversen, Discovery of high-performance low-cost n-type $Mg_3Sb_2$-based thermoelectric materials with multi-valley conduction bands. *Nat. Commun.* **8**, 13901 (2017). doi:10.1038/ncomms13901 Medline
25. J. Mao, J. Shuai, S. Song, Y. Wu, R. Dally, J. Zhou, Z. Liu, J. Sun, Q. Zhang, C. Dela Cruz, S. Wilson, Y. Pei, D. J. Singh, G. Chen, C.-W. Chu, Z. Ren, Manipulation of ionized impurity scattering for achieving high thermoelectric performance in n-type $Mg_3Sb_2$-based materials. *Proc. Natl. Acad. Sci. U.S.A.* **114**, 10548–10553 (2017). doi:10.1073/pnas.1711725114 Medline
26. J. Mao, Y. Wu, S. Song, Q. Zhu, J. Shuai, Z. Liu, Y. Pei, Z. Ren, Defect Engineering for Realizing High Thermoelectric Performance in n-Type $Mg_3Sb_2$ -Based Materials. *ACS Energy Lett.* **2**, 2245–2250 (2017). doi:10.1021/acsenergylett.7b00742
27. J. Shuai, J. Mao, S. Song, Q. Zhu, J. Sun, Y. Wang, R. He, J. Zhou, G. Chen, D. J. Singh, Z. Ren, Tuning the carrier scattering mechanism to effectively improve the thermoelectric properties. *Energy Environ. Sci.* **10**, 799–807 (2017). doi:10.1039/C7EE00098G
28. T. Kanno, H. Tamaki, H. K. Sato, S. D. Kang, S. Ohno, K. Imasato, J. J. Kuo, G. J. Snyder, Y. Miyazaki, Enhancement of average thermoelectric figure of merit by increasing the grain-size of $Mg_{3.2}Sb_{1.5}Bi_{0.49}Te_{0.01}$. *Appl. Phys. Lett.* **112**, 033903 (2018). doi:10.1063/1.5016488
29. S. Ohno, K. Imasato, S. Anand, H. Tamaki, S. D. Kang, P. Gorai, H. K. Sato, E. S. Toberer, T. Kanno, G. J. Snyder, Phase Boundary Mapping to Obtain n-type Mg3Sb2-Based Thermoelectrics. *Joule* **2**, 141–154 (2018). doi:10.1016/j.joule.2017.11.005
30. K. Imasato, S. D. Kang, S. Ohno, G. J. Snyder, Band engineering in $Mg_3Sb_2$ by alloying with $Mg_3Bi_2$ for enhanced thermoelectric performance. *Mater. Horiz.* **5**, 59–64 (2018). doi:10.1039/C7MH00865A
31. J. J. Kuo, S. D. Kang, K. Imasato, H. Tamaki, S. Ohno, T. Kanno, G. J. Snyder, Grain boundary dominated charge transport in $Mg_3Sb_2$ -based compounds. *Energy Environ. Sci.* **11**, 429–434 (2018). doi:10.1039/C7EE03326E
32. R. Shu, Y. Zhou, Q. Wang, Z. Han, Y. Zhu, Y. Liu, Y. Chen, M. Gu, W. Xu, Y. Wang, W. Zhang, L. Huang, W. Liu, Mg $_{3+\delta}$ Sb $_x$ Bi $_{2-x}$ Family: A Promising Substitute for the State-of-the-Art n-Type Thermoelectric Materials near Room Temperature. *Adv. Funct. Mater.* **29**, 1807235 (2019). doi:10.1002/adfm.201807235
33. K. Imasato, S. D. Kang, G. J. Snyder, Exceptional thermoelectric performance in $Mg_3Sb_{0.6}Bi_{1.4}$ for low-grade waste heat recovery. *Energy Environ. Sci.* **12**, 965–971 (2019). doi:10.1039/C8EE03374A
34. V. Ponnambalam, D. T. Morelli, On the Thermoelectric Properties of Zintl Compounds Mg3Bi2−x Pn x (Pn = P and Sb). *J. Electron. Mater.* **42**, 1307–1312 (2013). doi:10.1007/s11664-012-2417-7
35. J. Xin, G. Li, G. Auffermann, H. Borrmann, W. Schnelle, J. Gooth, X. Zhao, T. Zhu, C. Felser, C. Fu, Growth and transport properties of Mg3X2 (X = Sb, Bi) single crystals. *Mater. Today Phys.* **7**, 61–68 (2018). doi:10.1016/j.mtphys.2018.11.004
36. T. R. Chang, I. Pletikosic, T. Kong, G. Bian, A. Huang, J. Denlinger, S. K. Kushwaha, B. Sinkovic, H.-T. Jeng, T. Valla, W. Xie, R. J. Cava, Realization of a Type-II Nodal-Line Semimetal in $Mg_3Bi_2$. *Adv. Sci.* **6**, 1800897 (2018). doi:10.1002/advs.201800897 Medline
37. X. Zhang, L. Jin, X. Dai, G. Liu, Topological Type-II Nodal Line Semimetal and Dirac Semimetal State in Stable Kagome Compound $Mg_3Bi_2$. *J. Phys. Chem. Lett.* **8**, 4814–4819 (2017). doi:10.1021/acs.jpclett.7b02129 Medline
38. H. J. Goldsmid, *Introduction to thermoelectricity*, vol. 121. (Springer Science+Business Media, 2009).
39. H. J. Goldsmid, J. W. Sharp, Estimation of the thermal band gap of a semiconductor from Seebeck measurements. *J. Electron. Mater.* **28**, 869–872 (1999). doi:10.1007/s11664-999-0211-y
40. J. Schmitt, Z. M. Gibbs, G. J. Snyder, C. Felser, Resolving the true band gap of ZrNiSn half-Heusler thermoelectric materials. *Mater. Horiz.* **2**, 68–75 (2015). doi:10.1039/C4MH00142G
41. Z. M. Gibbs, H.-S. Kim, H. Wang, G. J. Snyder, Band gap estimation from temperature dependent Seebeck measurement—Deviations from the 2e|S|maxTmax relation. *Appl. Phys. Lett.* **106**, 022112 (2015). doi:10.1063/1.4905922
42. B. Abeles, S. Meiboom, Galvanomagnetic Effects in Bismuth. *Phys. Rev.* **101**, 544–550 (1956). doi:10.1103/PhysRev.101.544
43. B. Chandrasekhar, The seebeck coefficient of bismuth single crystals. *J. Phys. Chem. Solids* **11**, 268–273 (1959). doi:10.1016/0022-3697(59)90225-2
44. C. F. Gallo, B. S. Chandrasekhar, P. H. Sutter, Transport Properties of Bismuth Single Crystals. *J. Appl. Phys.* **34**, 144–152 (1963). doi:10.1063/1.1729056
45. A. L. Jain, Temperature Dependence of the Electrical Properties of Bismuth-Antimony Alloys. *Phys. Rev.* **114**, 1518–1528 (1959). doi:10.1103/PhysRev.114.1518
46. Q. Zhu, S. Song, H. Zhu, Z. Ren, Realizing high conversion efficiency of Mg3Sb2-based thermoelectric materials. *J. Power Sources* **414**, 393–400 (2019). doi:10.1016/j.jpowsour.2019.01.022
47. P. Giannozzi, S. Baroni, N. Bonini, M. Calandra, R. Car, C. Cavazzoni, D. Ceresoli, G. L. Chiarotti, M. Cococcioni, I. Dabo, A. Dal Corso, S. de Gironcoli, S. Fabris, G. Fratesi, R. Gebauer, U. Gerstmann, C. Gougoussis, A. Kokalj, M. Lazzeri, L. Martin-Samos, N. Marzari, F. Mauri, R. Mazzarello, S. Paolini, A. Pasquarello, L. Paulatto, C. Sbraccia, S. Scandolo, G. Sclauzero, A. P. Seitsonen, A. Smogunov, P. Umari, R. M. Wentzcovitch, QUANTUM ESPRESSO: A modular and open-source software project for quantum simulations of materials. *J. Phys. Condens. Matter* **21**, 395502 (2009). doi:10.1088/0953-8984/21/39/395502 Medline
48. K. Uemura, in *CRC Handbook of Thermoelectrics,* D. M. Rowe, Ed. (CRC, 1995).

## ACKNOWLEDGMENTS

We thank Q. Zhu and D. Z. Wang for assistance with the experiments, and C. Chen and Q. Zhang for supplying the commercial n-type $Bi_2Te_{3-x}Se_x$ ingot. **Funding:** Z.R. received a Humboldt Research Award from the Alexander von Humboldt Foundation. K. Nielsch at IFW in Dresden, Germany, supported part of the work. **Author contributions:** J.M. synthesized the samples and designed and performed experiments under Z.R.'s guidance. J.M. performed the data analysis and modeling. J.M. and H.Z. conducted the cooling measurements. L.Z. and G.G. helped with the thermoelectric characterization. Z.D. performed the first-principles calculations. J.M. wrote the manuscript. All authors contributed to

discussing the results and commenting on the manuscript. The project was directed and supervised by G.C. and Z.R. **Competing interests:** Z.R. and J.M. have filed a provisional patent application on the work described here. **Data and materials availability:** All data are available in the manuscript and supplementary materials.

## SUPPLEMENTARY MATERIALS

www.sciencemag.org/cgi/content/full/science.aax7792/DC1
Materials and Methods
Supplementary Text
Figs. S1 to S8
Tables S1 and S2
References (*46*–*48*)

22 April 2019; accepted 8 July 2019
Published online 18 July 2019
10.1126/science.aax7792

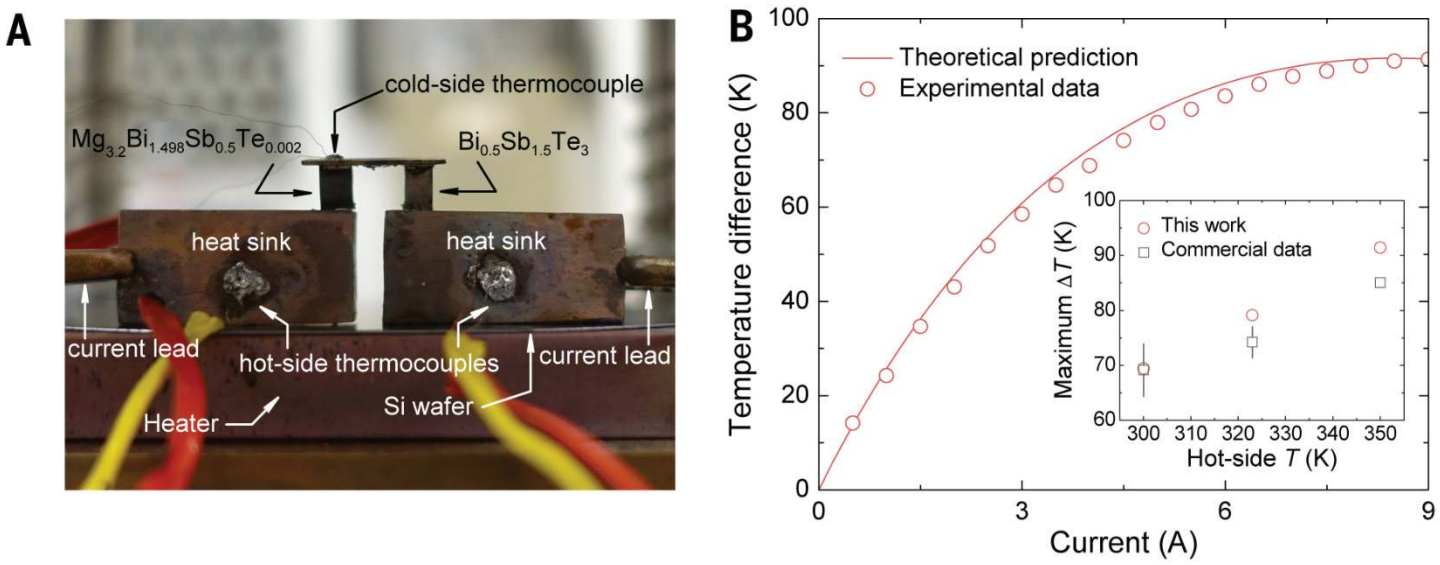


**Fig. 1. Thermoelectric cooling measurement.** (**A**) Experimental setup for the thermoelectric cooling measurement with a unicouple consisting of p-type $Bi_{0.5}Sb_{1.5}Te_3$ and n-type $Mg_{3.2}Bi_{1.498}Sb_{0.5}Te_{0.002}$. (**B**) Electrical current dependent *T* difference ($\Delta T$) between the hot and cold sides at the hot-side *T* of 350 K. The inset showed the comparison of hot-side *T* dependent maximum $\Delta T$ between our unicouple and commercial data. The commercial data were taken from table S2.

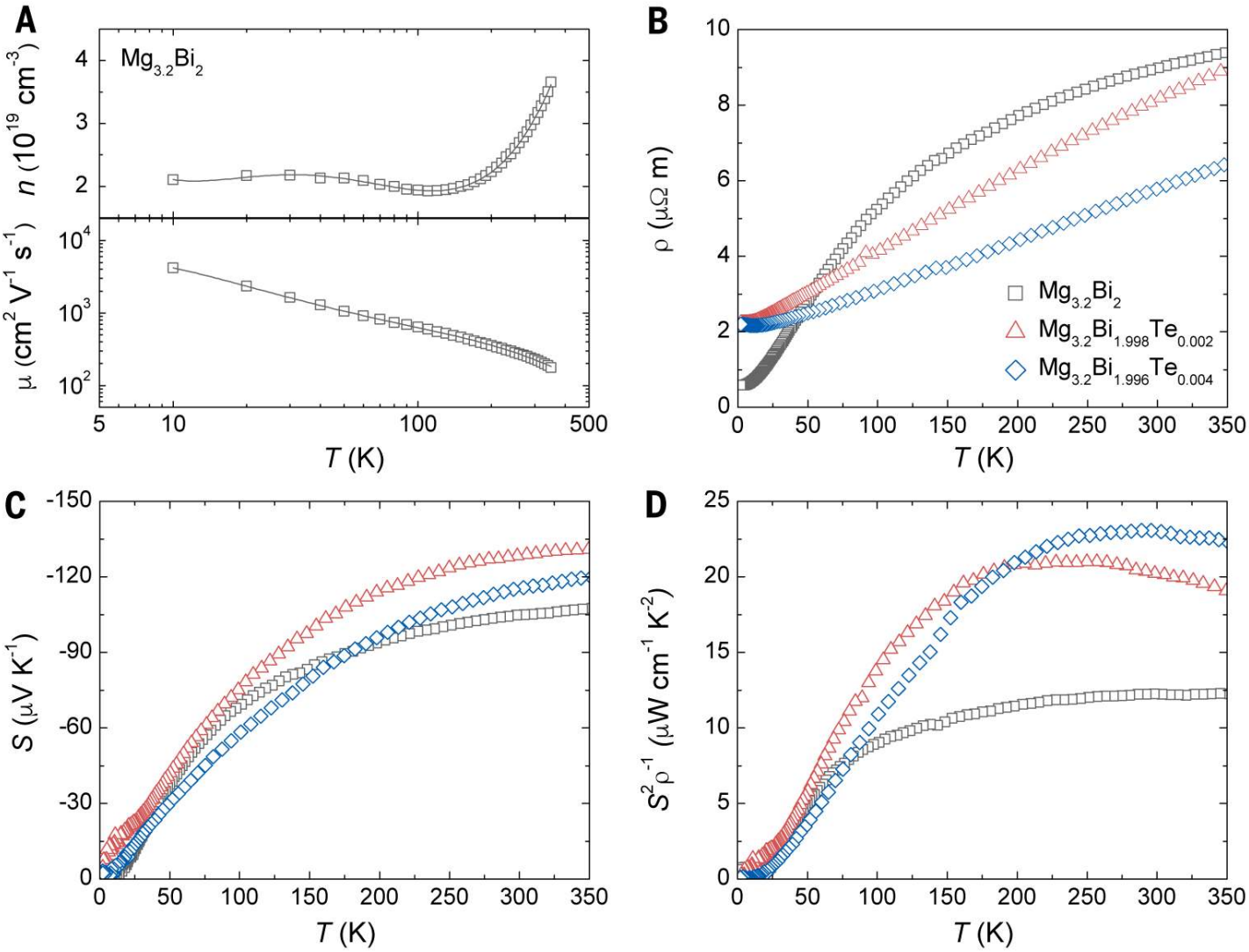


**Fig. 2. Electronic thermoelectric properties of $Mg_{3.2}Bi_{2-x}Te_x$.** (**A**) Carrier concentration (upper panel) and mobility (lower panel) of $Mg_{3.2}Bi_2$. (**B**) Electrical resistivity. (**C**) Seebeck coefficient. (**D**) Power factor.

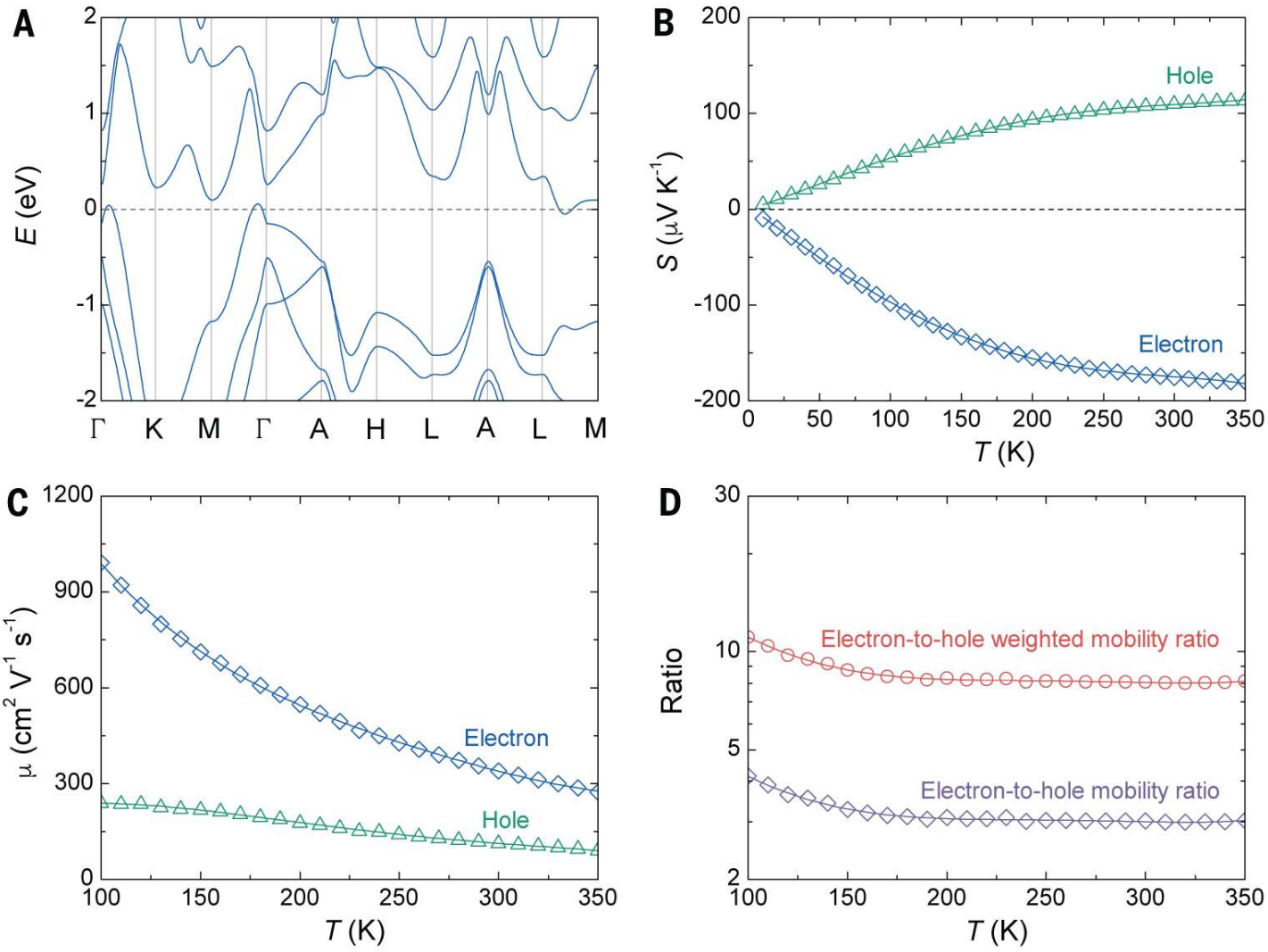


**Fig. 3. Band structure and transport properties of $Mg_{3.2}Bi_2$.** (**A**) Calculated band structure of $Mg_3Bi_2$ with the band overlap shifted to -0.1 eV. (**B**) Comparison of partial Seebeck coefficients between electrons and holes. (**C**) Comparison of mobilities between electrons and holes. (**D**) Electron-to-hole mobility ratio and electron-to-hole weighted mobility ratio.

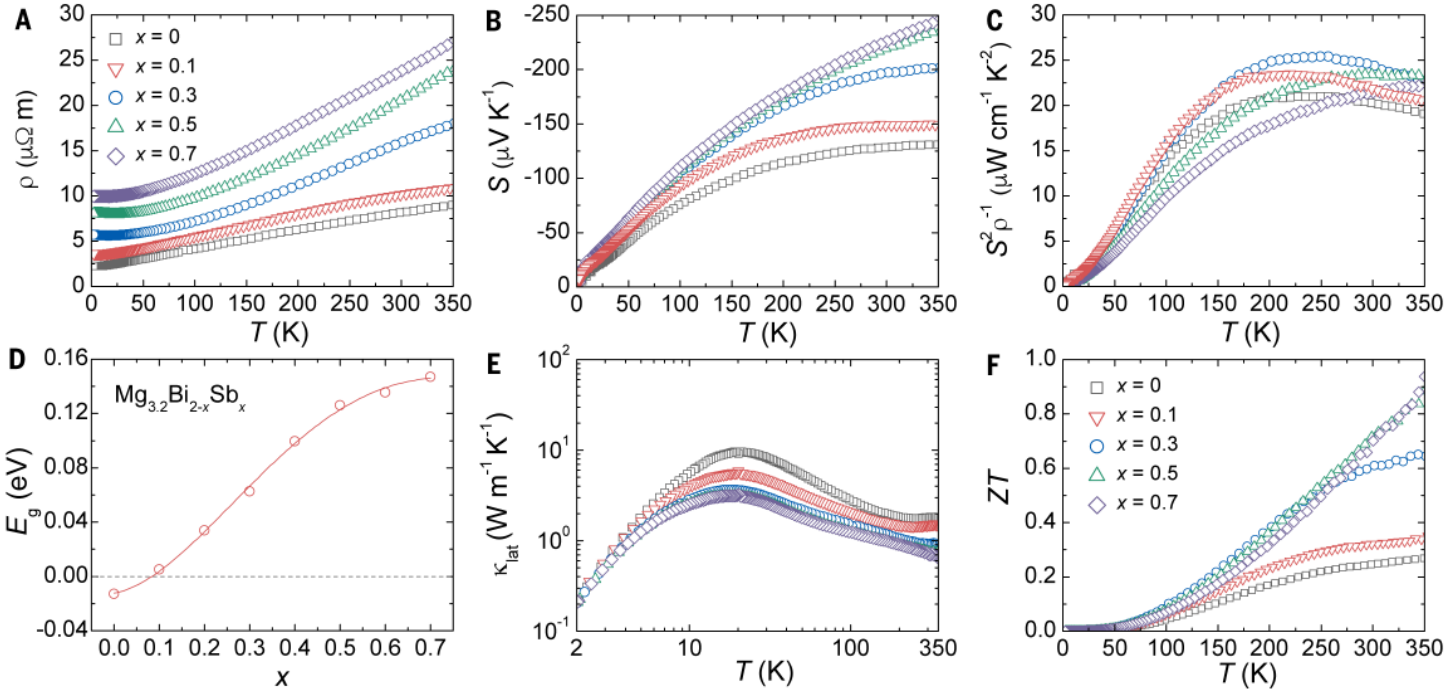


**Fig. 4. Thermoelectric properties of $Mg_{3.2}Bi_{1.998-x}Sb_xTe_{0.002}$.** (**A**) Electrical resistivity. (**B**) Seebeck coefficient. (**C**) Power factor. (**D**) Estimated bandgap of undoped $Mg_{3.2}Bi_{2-x}Sb_x$. (**E**) Lattice thermal conductivity. (**F**) *ZT*. The measurement errors of $Mg_{3.2}Bi_{1.498}Sb_{0.5}Te_{0.002}$ were shown in fig. S18.